

## Superintense laser-driven photon activation analysis

Francesco Mirani <sup>1</sup>✉, Daniele Calzolari <sup>2</sup>, Arianna Formenti <sup>1</sup> & Matteo Passoni<sup>1</sup>

Laser-driven radiation sources are attracting increasing attention for several materials science applications. While laser-driven ions, electrons and neutrons have already been considered to carry out the elemental characterization of materials, the possibility to exploit high-energy photons remains unexplored. Indeed, the electrons generated by the interaction of an ultra-intense laser pulse with a near-critical material can be turned into high-energy photons via bremsstrahlung emission when shot into a high-Z converter. These photons could be effectively exploited to perform Photon Activation Analysis (PAA). In the present work, laser-driven PAA is proposed and investigated. We develop a theoretical approach to identify the optimal experimental conditions for laser-driven PAA in a wide range of laser intensities. Lastly, exploiting the Monte Carlo and Particle-In-Cell tools, we successfully simulate PAA experiments performed with both conventional accelerators and laser-driven sources. Under high repetition rate operation (i.e. 1–10 Hz) conditions, the ultra-intense lasers can allow performing PAA with performances comparable with those achieved with conventional accelerators. Moreover, laser-driven PAA could be exploited jointly with complementary laser-driven materials characterization techniques under investigation in existing laser facilities.

<sup>1</sup>Politecnico di Milano, Milan, Italy. <sup>2</sup>CERN, Geneva, Switzerland. ✉email: [francesco.mirani@polimi.it](mailto:francesco.mirani@polimi.it)

Photon activation analysis (PAA)<sup>1–3</sup> is a nondestructive materials characterization technique that exploits high-energy photons to retrieve the elemental composition of a large variety of samples. During the irradiation time, photons interact with the sample under study, inducing photonuclear reactions. After a cooling period (i.e., rest time), delayed characteristic  $\gamma$ -rays are emitted and detected. These  $\gamma$ -rays are exploited to reconstruct the sample composition. From the knowledge of the characteristic  $\gamma$ -ray energy, the nuclear reaction, and the decay channel, the parent element is identified. Moreover, taking into account the number of  $\gamma$ -rays, the concentrations of the elements are reconstructed as well. Often, multiple measurements are performed after stepwise increasing the rest time to avoid spectral interference by short-lived nuclides. Because several physical quantities (e.g., the nuclear cross sections) and experimental parameters are not well known a priori, the elemental concentration reconstruction is performed exploiting a comparative (or calibration) material of known composition, which is co-irradiated with the sample. The primary photons are generated through the interaction of a high-energy (e.g., 20–30 MeV) electron beam with an mm-thick converter material having a high atomic number (e.g., tungsten). The primary electron beam is provided by a high-power linear accelerator, microtron, or betatron with a delivered current of  $\sim 10 \mu\text{A}$ . Exploiting bremsstrahlung (BS) emission, about 50% of the primary electron energy is converted into photons whose energies range from zero to that of the primary electrons<sup>4</sup>. The conventional PAA irradiation setup, some examples of photonuclear cross sections, and a BS energy spectrum are reported in Fig. 1. PAA can be used jointly to well-established materials characterization techniques like ion beam analysis (IBA)<sup>5</sup>, secondary ion mass spectrometry (SIMS)<sup>6</sup>, and energy-dispersive X-ray (EDX)<sup>7</sup> spectroscopy. Indeed, while IBA, SIMS, and EDX are suitable for the characterization of the material surface (i.e., from nanometers up to tens of micrometers depth), PAA allows probing the bulk composition of large samples (100s of grams or more). Depending on the material composition, irradiation requirements

and available primary sources, it is also complementary to other bulk analysis techniques as neutron activation analysis (NAA)<sup>3,8–10</sup>. Nowadays, PAA is routinely exploited for environmental<sup>11</sup>, biological<sup>12</sup>, geochemical<sup>10</sup>, archeological<sup>13</sup>, and industrial studies<sup>14</sup>.

Despite the great PAA analytical capabilities, the electron accelerators employed for decades have been characterized by large costs and size, with strong limitations to the widespread use of this technique. Laser-driven particle sources<sup>15–19</sup> may represent a promising alternative to conventional accelerators. They rely on the interaction of a super-intense ( $I > 10^{18} \text{W cm}^{-2}$ ) and ultra-fast laser pulse (few J,  $\sim 10$  fs) with a target to generate high-energy particles. For instance, when micrometric solid foils are exploited, electrons, and ions (mainly protons) are accelerated via the so-called target normal sheath acceleration (TNSA) mechanism. The collectively accelerated particles are characterized by ultra-fast dynamics and broad energy spectra. Interestingly, the generated particle type and properties can be tuned by acting on the laser parameters and target configuration. As a consequence, these sources are potential multifunctional tools for several applications in materials and nuclear science<sup>20</sup>. For instance, laser-driven protons, electrons, and neutrons accelerated exploiting 10–100 TW class lasers can be exploited for particle-induced X-ray emission (PIXE)<sup>21–23</sup>, energy-dispersive X-ray (EDX) spectroscopy<sup>23</sup>, and fast neutron spectroscopy<sup>24</sup>.

Advanced target configurations like very thin (i.e.,  $\sim 100$  nm) metallic foils<sup>25</sup>, reduced mass targets<sup>26</sup>, grating targets<sup>27</sup>, and double-layer targets (DLTs)<sup>28–30</sup> have proved to be a viable strategy to enhance the number and energy of the accelerated electrons and ions without having to increase the laser intensity. Notably, DLTs allow achieving the highest absorption of laser energy<sup>31</sup>. They are constituted by a micrometric thick foil coated with a near-critical density layer (e.g., a carbon foam<sup>32</sup> or nanotubes<sup>33</sup>). During the interaction, the laser pulse is greatly absorbed by the electrons in the near-critical layer through volumetric heating<sup>34</sup>. In recent works<sup>35–37</sup>, exploiting near-critical targets and  $\sim 100$  TW class lasers, even if using quite

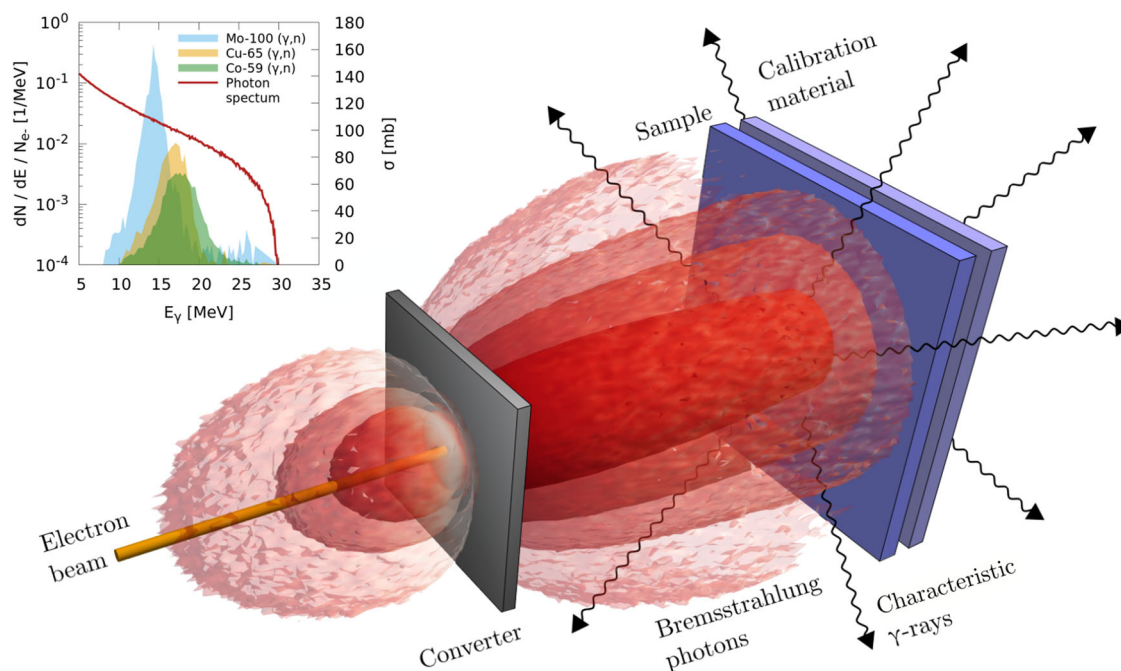


**Fig. 1 Conceptual setup of photon activation analysis.** The red line is the bremsstrahlung photon energy spectrum obtained from a Fluka simulation performed with 30 MeV monoenergetic electrons and a W converter having a thickness equal to 3 mm. The inset graph reports some examples of  $(\gamma, n)$  photonuclear cross sections (from the evaluated nuclear data file (ENDF) database<sup>67</sup>).

different laser drivers with longer pulses and higher energies (100 fs, 100 J), the possibility to accelerate electron bunches with maximum energy up to 80 MeV and total accelerated charge of several  $\mu\text{C}$  was demonstrated. Electrons can be converted into bremsstrahlung photons able to activate materials. Together with Monte Carlo (MC) simulations, the activation has been exploited as a diagnostic tool for the primary photon and electron beams<sup>36,38,39</sup>. An alternative, extensively investigated strategy for high-energy electrons production is to use under-critical gas-jet targets and the wakefield acceleration (lwfa) mechanism<sup>40</sup>. In this case, exploiting  $\sim 10$ – $100$  TW lasers working at 1– $10$  Hz repetition rate, the accelerated electrons are quasi-monoenergetic with energies up to  $\sim\text{GeV}$  and accelerated charge of  $\sim 10$ – $100$  pC per bunch<sup>41–44</sup>. In addition, sub-TW class lasers (i.e., 10s mJ of energy) have been successfully exploited to perform lwfa at kHz repetition rate<sup>45</sup>. The energy of the electrons is of the order of  $\sim 10$  MeV with delivered currents of  $\sim 10$  nA. The conversion of lwfa electrons into bremsstrahlung radiation for applications<sup>46</sup> like imaging<sup>47</sup>, neutron production<sup>48</sup>, and integral ( $\gamma$ , n) cross-section measurements<sup>49</sup> have been proposed.

On the other hand, the possibility of performing PAA with photons generated from laser-driven electrons has not been considered yet. The main goal of this work is to numerically investigate this potential application of laser-driven electron sources. To this aim, even if both lwfa and near-critical solid targets are worthy of consideration, we focus on the second approach because of the higher delivered charge per laser shot. We consider a low-density material, e.g., a foam, for the electron acceleration, attached to an mm-thick W plate for the production of high-energy photons. Note that this peculiar DLT configuration is compatible with the experimental setup for ion acceleration based on thin solid targets. Therefore, another advantage over lwfa consists in the possibility of switching from the proton acceleration to photon production with minimum changes to the experimental apparatus. This could allow performing different materials characterization techniques that cannot be carried out with the same conventional accelerator (e.g., the surface analysis with PIXE and the bulk analysis with PAA).

This work has two objectives. The first one consists in the development of a theoretical description of PAA, performed with either conventional or laser-driven sources. This was achieved by exploiting Fluka<sup>50</sup> MC simulations and a proper theoretical description of laser-driven electrons acceleration in near-critical density media<sup>51</sup>. This theoretical description allows us to optimize the laser-driven source parameters to achieve maximum PAA performance. Moreover, the model is used to compare the laser-driven PAA capabilities with that accomplished exploiting conventional accelerators. The second goal of the work is to simulate specific PAA experiments through the MC tool. The simulations are carried out considering both monoenergetic and broad laser-driven like electron energy spectra. Moreover, the latter are described both with a simplified analytical description and performing a 3D particle-in-cell (PIC) simulation<sup>52,53</sup>. We provide the electron momenta distribution from the PIC as input to the MC simulation. This analysis shows that the model introduced in the first part of the work provides reliable results and that laser-driven sources may be effectively exploited for PAA studies.

## Results and discussion

### Theoretical models for conventional and laser-driven PAA.

One important goal of the present study is to compare the PAA performances, in terms of the emitted characteristic  $\gamma$ -ray signals, achievable with monoenergetic electron sources and laser-driven ones. To this aim, theoretical descriptions of both conventional

PAA and laser-driven PAA are required. The models must provide the sample activation rate for wide ranges of accelerator and laser operating parameters. In addition, the models have to take into account the optimal converter thickness (i.e., the thickness that maximizes the number of photonuclear reactions).

A theoretical description of PAA suitable for the mentioned purpose is not present in the literature. Therefore, we start considering monoenergetic electrons and we perform a parametric scan to determine the photonuclear reaction yield as a function of the electron energy and converter thickness. This quantity, which represents the number of activated nuclides in the sample per unit of incident electrons, is used to identify the optimal converter thickness. Then, we carry out the same scan considering electrons with exponential energy spectra, thus compatible with the electrons provided by a laser-driven source. Exploiting the model available from Pazzaglia et al.<sup>51</sup>, we introduce the main laser and target parameters in the description. The goal is to find the optimal target parameters (i.e., near-critical layer density and thickness) for the laser-driven electron source. Lastly, the theoretical frameworks developed for the conventional and laser-driven PAA are used to compare the performances of the techniques.

*Model for PAA with monoenergetic electrons.* Two fundamental ingredients for the evaluation of the PAA performances are the BS production of  $\gamma$ -rays and the probability to have photonuclear reactions. As far as the BS emission is concerned, the generated photon spectrum  $f(E) = (1/N_e)dN_\gamma/dE$  per unit of incident electron  $N_e$  can be obtained using analytical formulas<sup>54</sup> or MC simulations<sup>55</sup>. The first approach is very useful to provide quick estimates. However, it requires the adoption of simplifying assumptions which, in some cases, can lead to a nonacceptable degree of error. Accordingly, a MC description of the process is often demanded in several applications, as in the case of PAA studies<sup>56</sup>. Therefore, we performed a set of 49 MC simulations to evaluate the BS energy spectra obtained from different primary electron energies (i.e., 10, 15, 20, 25, 30, 35, and 40 MeV) and tungsten converter thicknesses (i.e., 1, 2, 3, 4, 5, 7, and 10 mm). The selected values cover the ranges usually exploited in PAA experiments. Some examples of the obtained  $\gamma$ -ray spectra are reported in Fig. 2(a),(b) for different primary electron energies and converter thicknesses, respectively.

Even if ( $\gamma$ , 2n), ( $\gamma$ , 3n), ( $\gamma$ , p) reactions can take place, the ( $\gamma$ , n) are the most commonly exploited for PAA purposes<sup>2</sup>. Therefore, that is the only kind of photonuclear event considered here. The cross sections are well described by a bell-shaped function centered approximately around 15–20 MeV (see Fig. 2(c)). The position of the maximum is weakly dependent on the isotope, and its magnitude can range from few tens up to hundreds of mbarn. We model the cross section as  $\sigma(E) = \sigma_{\text{int}}\tilde{\sigma}(E)$ , where  $\sigma_{\text{int}}$  is the total area and  $\tilde{\sigma}(E)$  is a normalized cross section described as a Gaussian function. A comparison between the  $\tilde{\sigma}(E)$  and experimental cross sections upon normalization is shown in Fig. 2(c). To generalize the discussion, we will exploit  $\tilde{\sigma}(E)$  instead of  $\sigma(E)$  in the remaining part of the work.

We evaluate the integral:

$$Y(E_e, l) = \int_E f(E_e, l; E) \times \tilde{\sigma}(E) dE \quad (1)$$

considering the BS spectra  $f(E)$  obtained from the MC simulations.  $Y(E_e, l)$  is the normalized reaction yields (i.e. per unit of electrons) for the different primary electron energies  $E_e$  and converter thicknesses  $l$ . To retrieve the value of  $Y(E_e, l)$  for the whole range of electron energies and thicknesses, we fit the discrete values with a fourth-order polynomial in the variables  $E_e$  and  $l$ . The resulting continuous function  $Y(E_e, l)$  is represented as

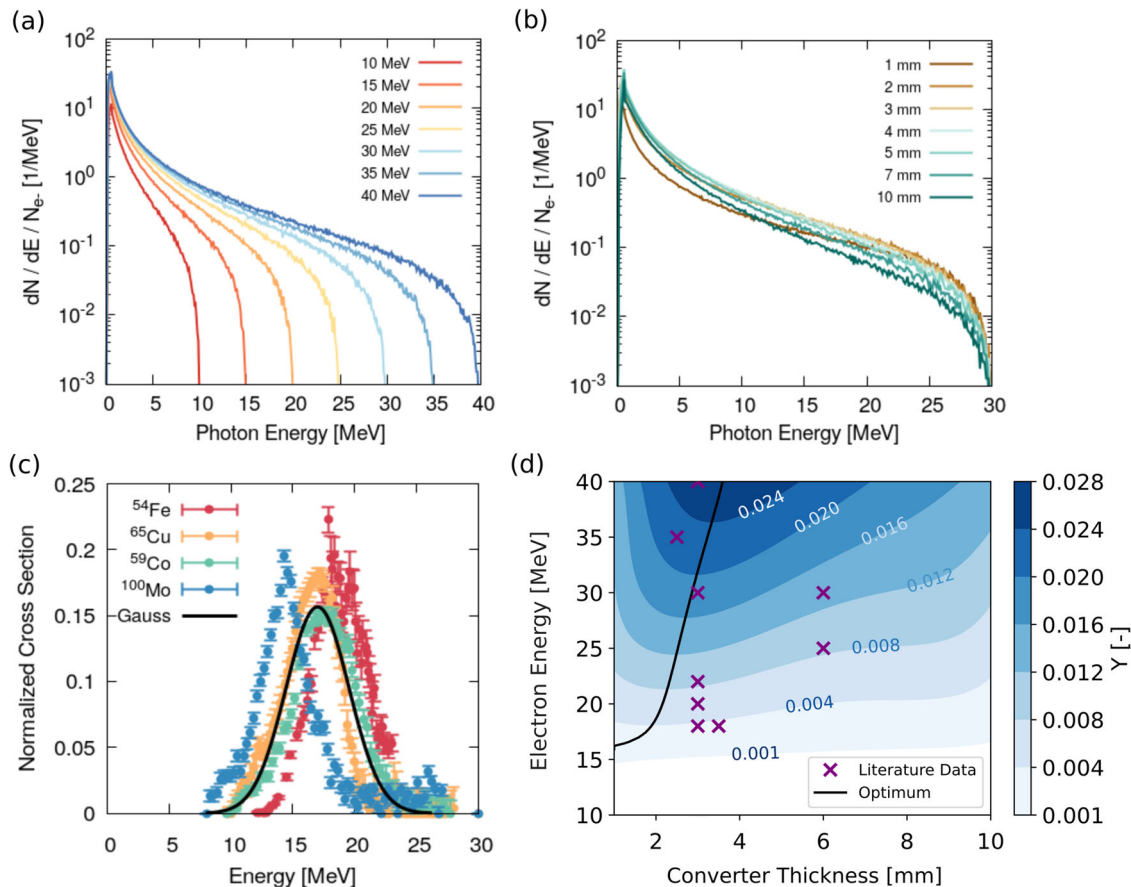


**Fig. 2 Parametric scan and model results for photon activation analysis (PAA).** **a** Photon energy spectra from Fluka simulations for different values of the primary electron energy and fixed converter thickness (i.e., 3 mm). **b** Photon energy spectra from Fluka simulations for different values of the converter thickness and fixed primary electron energy (i.e., 30 MeV). The spectra are normalized to the total number of primary electrons. **c** Comparison between a Gaussian function centered in 17 MeV, FWHM = 7 MeV and normalized experimental photonuclear cross sections. Both absolute values and uncertainties are retrieved from the ENDF database<sup>67</sup> and then normalized to the area subtended by the cross sections. **d** Contour plot showing the normalized yield as a function of the primary electron energy and converter thickness. The black line marks the locus of optimal converter thickness, while the purple markers correspond to working points from the literature<sup>56,68-74</sup>.

a blue contour plot in Fig. 2(d). Lastly, we evaluate the optimal converter thickness  $l_{\text{opt}}$  as a function of the incident electron energy from:

$$l_{\text{opt}}(E_e) = \arg \max_l Y(E_e, l) \quad (2)$$

and the corresponding values of normalized yields  $Y_{\text{max}}(E_e) = Y(E_e, l_{\text{opt}}(E_e))$ . The quantity  $l_{\text{opt}}(E_e)$ , obtained through the maximization, represents the converter thickness that provides the highest sample activation  $Y_{\text{max}}(E_e)$  for each electron energy. It is superimposed to the heat map in Fig. 2(d). In addition, we marked the points corresponding to some literature experimental conditions adopted in the past for PAA. We want to point out that the electron current  $I_e$ , which is an important operating parameter for PAA, is not considered here. This is due to the fact that the electron energy and current are considered as independent parameters and the optimal converter thickness can be obtained without taking into account the latter.

From the obtained results, we observe that the performances of PAA, expressed in terms of reaction yields, are weakly dependent on the adopted converter thickness. The optimum is between 2 and 4 mm and several converter thicknesses from literature are in this range. On the other hand, the dependence on electron energy is stronger. For the considered photonuclear cross-section parameters, the BS photons generated by electrons having

$E_e \leq 15$  MeV are not energetic enough to induce a significant amount of photonuclear reactions. Accordingly, the curve for the optimal thickness asymptotically tends to zero around  $\sim 15$  MeV of energy. Below this value, no BS photons useful for PAA are produced, whatever the value of the converter thickness.

While  $Y_{\text{max}}(E_e)$  will be exploited in the following to carry out the comparison between conventional and laser-driven PAA, the approach we propose here can be used for the converter design in future PAA experiments.

**Model for PAA with laser-driven electrons.** We consider laser-driven electrons characterized by exponential energy spectra with maximum energy equal to 40 MeV. With this choice of the cut-off, the electron energies, and therefore the generated BS spectra, fall in the region of nonvanishing photonuclear cross sections. The value is quite reasonable for sufficiently intense laser pulses (normalized laser intensity  $a_0 \geq 10$ ) and targets coated with a near-critical density layer<sup>30</sup>. However, since the electron spectrum is exponential, very few BS photons are produced in correspondence with the cut-off. Therefore, the exact value of the maximum electron energy has a negligible effect on the number of activated nuclei.

We carry out 35 MC simulations to retrieve the BS energy spectra for various electron temperatures  $T_e$  (i.e., 5, 10, 15, 20, and 25 MeV) and converter thicknesses (i.e. 1, 2, 3, 4, 5, 7, and



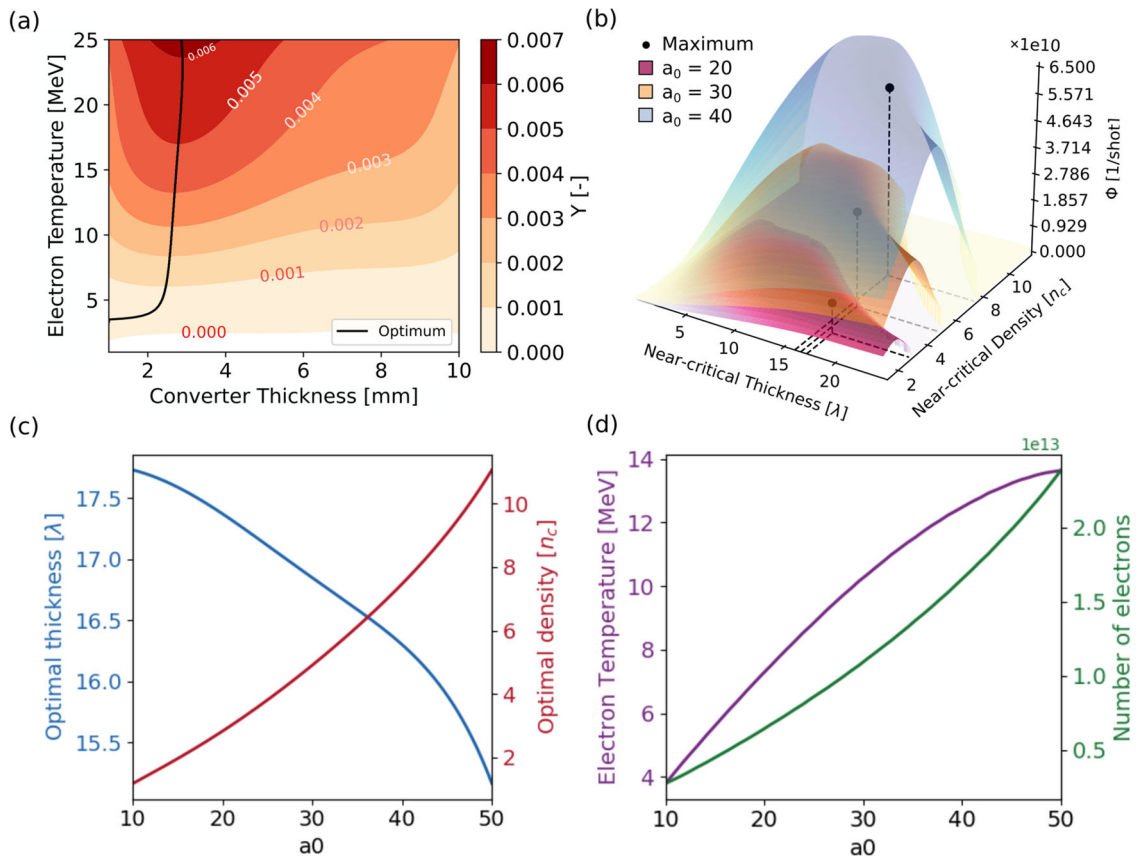


**Fig. 3 Parametric scan and model results for laser-driven photon activation analysis (PAA).** **a** Contour plot showing the normalized yield as a function of the laser-driven electron temperature and converter thickness. The black line marks the locus of optimal converter thickness. **b** Normalized yield per laser shot for three values of  $a_0$  (i.e., 20, 30, and 40) as a function of the target near-critical layer density and thickness. The positions of the maximum values are marked with black dots. **c** Trends for the optimal near-critical layer thickness and density as a function of  $a_0$ . **d** Trends for the electron temperature and the number of accelerated electrons per shot as a function of  $a_0$ .

10 mm). We exploit the same procedure described in the previous Section to find the normalized reaction yields for each value of  $T_e$  and  $l$ , as well as the optimal converter thickness  $l_{opt}(T_e)$  (see Fig. 3(a)).

To proceed, the maximum normalized yield  $Y_{max}(T_e)$  (i.e., the values corresponding to the optimal laser-driven PAA conditions) must be expressed in terms of the laser and target operating parameters. Here we consider the near-critical layer thickness  $r_{nc}$  and density  $n_{nc}$  of the target and the normalized laser intensity  $a_0$ . To this aim, we exploit the recently developed theoretical model from Pazzaglia et al.<sup>51</sup> (see the “Methods” Section for details). The model allows us to express the operating parameters in terms of the electron temperature and, therefore, to  $Y_{max}$ . In this case, the number of accelerated electrons per shot  $N_e$  is not decoupled from the temperature. Indeed, both  $T_e$  and  $N_e$  depend on the model parameters, here  $r_{nc}$ ,  $n_{nc}$ , and  $a_0$ . Therefore, the definition of the optimal laser-driven PAA conditions needs to be extended, including the number of accelerated electrons per shot. The quantity that will be further maximized is the normalized yield per laser shot:

$$\Phi(r_{nc}, n_{nc}, a_0) = Y_{max}(T_e(r_{nc}, n_{nc}, a_0)) \times N_e(r_{nc}, n_{nc}, a_0) \quad (3)$$

where  $T_e$  and  $N_e$  are related to  $r_{nc}$ ,  $n_{nc}$ , and  $a_0$  according to the mentioned model. In the model, we assume a linearly polarized laser pulse with normal incidence, wavelength  $\lambda = 0.8 \mu\text{m}$  and waist  $FWHM = 4.7 \mu\text{m}$ . The curves in Fig. 3(b) show the behavior of  $\Phi$  as a function of  $r_{nc}$  and  $n_{nc}$  for three values of  $a_0$ . Then, for a certain value of  $a_0$ , the optimal near-critical thickness, and density

are obtained from:

$$r_{opt}(a_0), n_{opt}(a_0) = \arg \max_{n_{nc}, r_{nc}} \Phi(r_{nc}, n_{nc}, a_0) \quad (4)$$

The corresponding values are marked in Fig. 3(b) as well.

We evaluate equation (4) for  $a_0$  ranging from 10 to 50. The resulting optimal target parameters are reported in Fig. 3(c). The thickness and density are in units of  $\lambda$  and critical density  $n_c$ , respectively. For each value of  $a_0$ , the reported  $r_{opt}$ , and  $n_{opt}$  maximize the activation of the sample. That maximization is the result of a trade-off between the accelerated electron temperature and number, which in turn affect the BS photon spectrum. The values of  $T_{e,opt}(a_0)$  and  $N_{e,opt}(a_0)$  are reported in Fig. 3(d). As expected, they monotonically increase with the intensity of the laser. We can also obtain the corresponding values for the maximum normalized yield per laser shot  $\Phi_{max}(r_{opt}(a_0), n_{opt}(a_0), a_0)$ .

*Comparison between conventional and laser-driven electron sources.* In the previous Sections, we have identified the optimal parameters for conventional PAA (i.e., the converter thickness as a function of the electron energy) and laser-driven PAA (i.e., the converter thickness, the near-critical layer thickness, and density as a function of the laser intensity). Now, the aim is to compare the performances of the PAA, in terms of sample activation rates, carried out with monoenergetic and laser-driven electron sources. For this reason, the normalized yields per impinging electrons  $Y_{max}(E_e)$  must be multiplied by the electron current  $I_e$  provided by the conventional accelerator. The result is the normalized

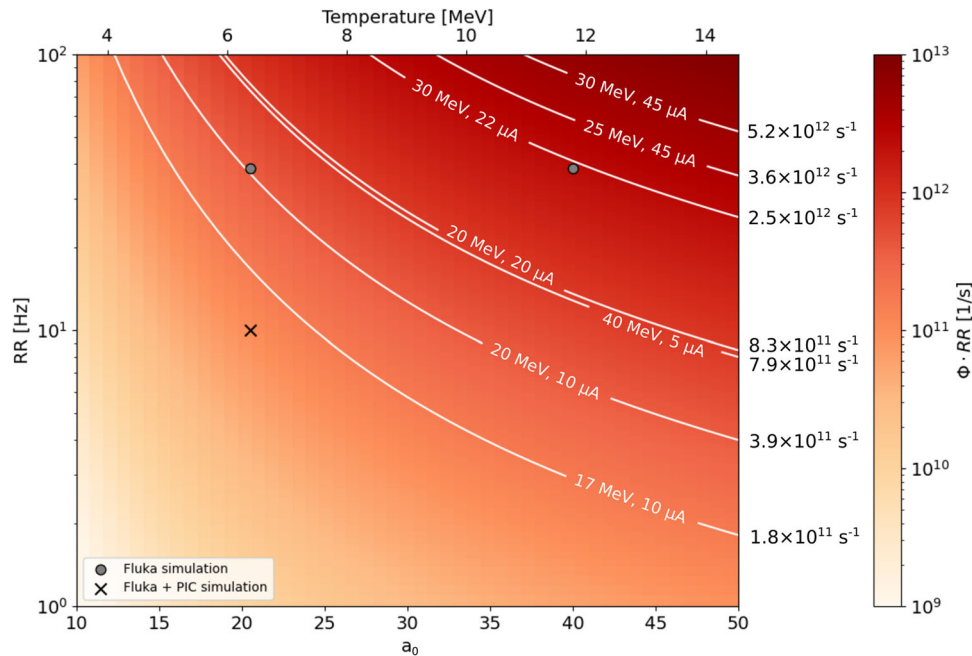


**Fig. 4 Comparison between laser-driven and monoenergetic sources for PAA.** The red color map represents the normalized activation rate obtained for laser-driven sources. The isolines correspond to the normalized activation rate that can be obtained with some existing conventional accelerators for PAA (reported electron energies and currents from literature<sup>68,71</sup>). The value of the normalized activation rate for each isoline is reported on the right side of the plot. The gray points identify the two selected experimental conditions for which the full PAA Monte Carlo simulations are performed. The cross marker identifies the laser parameters for the realistic laser-driven PAA simulation.

activation rate of the sample with conventional PAA. As far as the laser-driven source is concerned, the normalized activation rate is given by the product between the normalized yield per laser shot  $\Phi_{\max}(a_0)$  and the repetition rate RR. Note that, both in the case of conventional and laser-driven PAA, the normalized activation rates are retrieved considering the optimal converter thicknesses and near-critical layer parameters.

In Fig. 4, the behavior of the normalized activation rate  $\Phi_{\max}RR$  associated with laser-driven PAA is shown as a red color map for  $a_0$  and RR in the ranges 10–50 and 1–100 Hz, respectively. On the upper  $x$ -axis, we report the corresponding values of  $T_{e,\text{opt}}(a_0)$  obtained in the previous Section. The isolines represent specific monoenergetic sources identified by the energy and current of the primary electrons. Their positions are fixed by the relation  $\Phi_{\max}(a_0)RR = Y_{\max}(E_e)I_e$ . Therefore, each isoline for the monoenergetic source lies in correspondence with several possible equivalent laser systems. The reliability of the comparison will be carefully checked in the following Section. Here, we aim at discussing the feasibility of laser-driven PAA.

To generate enough BS photons to sufficiently activate the sample, both the laser intensity (thus the electron temperature) and the repetition rate must be taken into account. Indeed, the performances of laser-driven PAA will be given by a trade-off between these two parameters. The existing ultra-intense lasers already provide intensities in the entire range considered for  $a_0$ . However, the nominal repetition rate they can currently reach is 1–10 Hz<sup>57,58</sup>. Therefore, the upper region of the map in Fig. 4 (i.e., where some of the most powerful conventional accelerators for PAA are located) is not achievable yet. Nevertheless, considering the lower region of the map, we observe that 100s TW class laser and near-critical targets can approach the performances of, at least, some conventional accelerators for PAA.

To that end, operating at high repetition rates (HRR) for hour-long irradiation time is important. Nowadays, when solid targets are exploited, achieving HRR is challenging because of issues

related to the laser-target interaction. Indeed, fast target refreshing, positioning, alignment, and protection of both the optics and neighboring targets from the debris are demanded. Besides PAA, several potential applications of laser-driven radiation sources require high repetition rates and long-time operation. Therefore, many efforts have been done to satisfy the mentioned needs<sup>59</sup>. For instance, fast target delivery components<sup>60,61</sup> and rapid alignment systems<sup>62</sup> have been realized. Moreover, different strategies have been developed to protect the optical components from the debris<sup>59,63</sup>. To achieve the best laser-driven PAA performances, all those strategies must be implemented. Lastly, the near-critical layer present in our target configuration can be subject to damages because of the re-deposition of evaporated material. Thus, it should be equipped with a protective grid to preserve the regions adjacent to the interaction point.

It is worth noting that the distance between the sample and converter, the irradiation time, rest time, and characteristic  $\gamma$ -ray measurement time are assumed to be equal in laser-driven and conventional PAA. This choice allows making a general comparison. However, these setup parameters could be adjusted accordingly to the specific irradiation condition and sample material. For instance, a possible path to improve the laser-driven PAA performances is to reduce the converter-sample distance and, therefore, increase the photon flux on the sample. This possibility is further discussed in the following Section.

We also want to point out that the research in ultra-intense laser technology is very active. In this respect, a further improvement in the performances and a reduction of dimensions and costs are foreseen in the following years. Thus, laser-driven electron sources could be on their way to becoming competitive with conventional accelerators for applications like PAA.

**PAA simulations with monoenergetic and laser-driven electrons.** The second part of this work is focused on the Fluka MC

simulation of PAA experiments performed with both monoenergetic and laser-driven sources. The simulations take into account the generation of BS photons, the activation of the sample and standard material, the decay and delayed emission of characteristic  $\gamma$ -rays. A detailed description of the MC simulations is provided in the “Methods” Section.

We consider five experimental conditions, two of which (called S1 and S2 from here on) involve monoenergetic electron sources with energies of 30 and 20 MeV and currents equal to 22 and 10  $\mu$ A, respectively. For these two cases, we simulate the equivalent PAA experiments (i.e., S3 and S4) performed with laser-driven sources. Accordingly to the model described in the previous Section, they should provide the same values of normalized activation rate. The considered experimental conditions are marked as gray points in Fig. 4. The laser-driven electron energy spectra are modeled as pure exponential functions with cut-off energies of 40 MeV. The motivations behind the choice of this maximum electron energy value are reported in the previous Section. The goal is to compare the number of emitted characteristic  $\gamma$ -rays for all four cases and check the reliability of the comparison in the previous Section.

Then, the feasibility of the approach developed for the design of a laser-driven PAA experiment must be tested on one realistic case study. Moreover, assessing whether the elemental composition of the sample can be obtained with less demanding laser requirements is crucial. These are the objectives of the last simulation (i.e., S5) for which the laser parameters are identified with a cross marker in Fig. 4. The near-critical layer and converter parameters are selected accordingly to the analysis presented in the previous Section. Since S5 must be a test-bed investigation in which all steps of the laser-driven PAA experiment are modeled at best, the electron energy spectrum and angular divergence are obtained from a 3D particle-in-cell simulation. Indeed, the PIC simulation allows knowing the momenta distribution of the electrons consistently with the physics in play during the laser-foam interaction.

The sample and standard compositions and dimensions are the same for all the simulations. They are compatible with the content of a bronze sculpture (1550–1400 BC) analyzed by Prompt Gamma Activation analysis and Neutron Imaging<sup>64</sup>. The sample and standard contain several elements (see the “Methods” Section). As far as the activation is concerned, we focus on Cu, Na, Fe, Pb, Ni, and Ca. For each PAA simulated experiment, we consider three different cooling times and measurement times. A summary of the main parameters for all the simulations is provided in Table 1.

Lastly, it is worth mentioning that, both in the case of conventional and laser-driven PAA, the converter is not thick enough to stop all the electrons. The surviving electrons can cause the overheating of delicate materials. A detailed investigation of this condition is beyond the aims of this work and, therefore, is not considered in the simulations. Nevertheless, it can be avoided by adding a light metal filter<sup>3</sup> or standard beam optics (e.g., a dipole magnet) between the converter and the sample.

*Test of the comparison between conventional and laser-driven PAA.* From the MC simulations, we retrieve the characteristic  $\gamma$ -ray energy spectra collected during the measurement times, following the irradiation and rest times. An example of the spectrum, from the S1 simulation and recorded after a rest time of 12 h, is shown in Fig. 5(a). The positions of the considered characteristic peaks for the various elements are highlighted. To assess the feasibility of the comparison presented in the first part of the work, we perform the ratio between the peak intensities obtained in the simulations S1, S2, S3, and S4 for the various elements. Then, we compare the simulated ratios with those predicted by the theoretical model. We perform the intensity ratios because the results are independent of several parameters like the sample mass, thickness, and elemental concentrations, the specific values of  $\bar{\sigma}$ , the irradiation, measurement, and cooling times. Therefore, the ratios between line intensities (from the MC) can be directly compared with the ratios between normalized activation rates (from the theoretical model).

We start considering the ratios between the intensities of simulations S1/S2 (i.e., the monoenergetic electron sources) and S3/S4 (i.e., the laser-driven electron sources). They are plotted in Fig. 5(b) as blue and yellow points for all the elements. The ratios involve simulations performed in correspondence of different points of the map in Fig. 4. The predicted result is 6.2 considering a normalized cross section  $\bar{\sigma}(E)$  centered in 17 MeV (the continuous red line in Fig. 5(b)). Assuming a cross section centered in 15 and 20 MeV, the expected ratios result in 4.9 and 9.8, respectively (the dashed lines in Fig. 5(b)). Clearly, the expected ratio, and therefore the predicted performances of laser-driven PAA, depends on the choice of the parameters for the cross section. This is also confirmed by the different ratios obtained for the various elements. Nevertheless, all the points lie within the interval identified by the lower and upper values adopted for the definition of the cross section. Therefore, for both monoenergetic and laser-driven electrons, the model predicts satisfactorily how the characteristic peak intensities scale for sources with different operating parameters.

**Table 1 Summary of the parameters adopted in the simulations. PIC stands for particle-in-cell.**

Source	Monoenergetic		Laser-driven		
	S1	S2	S3	S4	S5
Electron energy ( $E_e$ ) [MeV]	30	20	-	-	-
Electron current ( $I$ ) [ $\mu$ A]	22	10	-	-	-
Laser intensity ( $a_0$ ) [-]	-	-	40	20.5	20.5
Laser repetition rate (RR) [Hz]	-	-	38.6	38.6	10
Near-critical density ( $n_{opt}$ ) [ $n_c$ ]	-	-	7.5	2.92	2.92
Near-critical thickness ( $r_{opt}$ ) [ $\lambda$ ]	-	-	16.3	17.34	17.34
Electron temperature ( $T_e$ ) [MeV]	-	-	12.5	7.5	PIC
Electrons per shot ( $N_e$ ) [-]	-	-	$1.6 \times 10^{13}$	$6.4 \times 10^{12}$	PIC
Converter thickness ( $t$ ) [mm]	3	2.41	2.73	2.58	2.58
Irradiation time ( $t_i$ ) [h]	3	3	3	3	3
Rest times ( $t_r$ ) [d]	0.5, 7, 30	0.5, 7, 30	0.5, 7, 30	0.5, 7, 30	0.5, 7, 30
Measurement times ( $t_m$ ) [h]	2, 8, 24	2, 8, 24	2, 8, 24	2, 8, 24	2, 8, 24

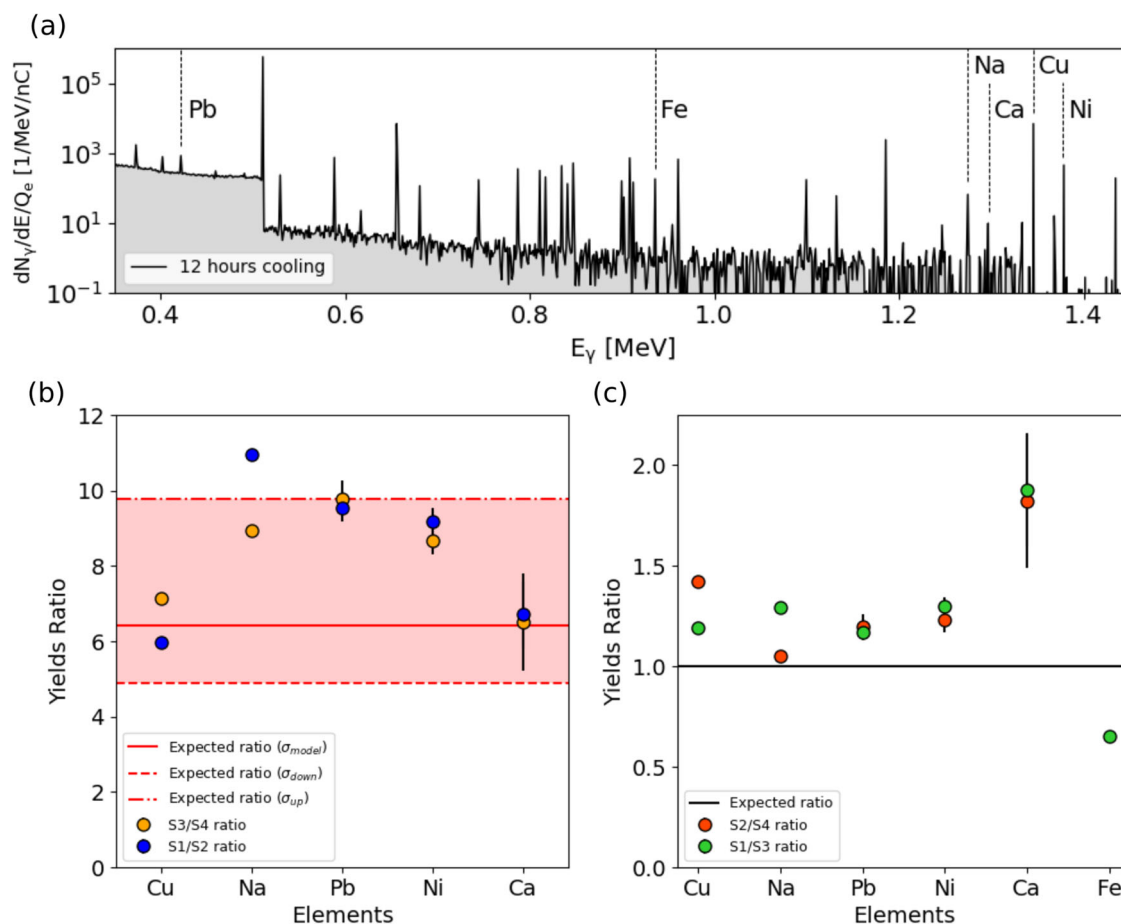


**Fig. 5 Comparison between Monte Carlo simulations and model results.** **a** Photon energy spectrum from Monte Carlo simulation S1 was obtained from sample irradiation after 12 h rest time and for 3 h measurement time. The considered characteristic  $\gamma$ -ray peaks for the elements are identified by the dashed lines. **b** Ratio between the intensities of simulations S1/S2 (blue point) and S3/S4 (yellow points) for each element. The continuous red line corresponds to the ratio predicted by the model assuming a normalized cross section centered at 17 MeV. The dashed upper and lower red lines correspond to the ratio predicted by the model assuming normalized cross sections centered in 20 and 15 MeV, respectively. **c** Ratio between the intensities of simulations S1/S3 (green points) and S2/S4 (red points) for each element. The black line corresponds to the value predicted by the model. The error bars are evaluated as two times the standard deviation of the data collected with the Monte Carlo.

In Fig. 5(c), the ratio between the intensities of simulations S1/S3 and S2/S4 (i.e., the monoenergetic sources over the equivalent laser-driven ones) are shown. In this case, the expected ratio is equal to 1 (the continuous black line). With the only exception of Ca, all the points lie in a region close to the expected value. On average, the discrepancy is of the order of 20%. Therefore, the comparison allows us to establish an equivalence between monoenergetic and laser-driven sources within an acceptable range of reliability.

Lastly, it is worth mentioning that the points associated with the Fe peak are not present in Fig. 5(b). This is due to the fact that the generated BS photons in simulations S2 and S4 are not energetic enough to induce sufficient  $(\gamma, n)$  reactions.

**Combined PIC and Monte Carlo simulation of laser-driven PAA.** The last laser-driven PAA simulation (i.e., S5) involves laser parameters compatible with the state-of-the-art technology<sup>57</sup>, while the near-critical target and converter properties are optimized according to the results presented in the first part of the work. The main parameters are summarized in the last column of Table 1. As already mentioned in the “Introduction” Section, we consider a two-layer structure where the near-critical medium is attached to the high-Z material. For our purposes, this choice has several advantages.

The electrons accelerated by the laser in the first layer are directly injected inside the converter. The main advantage is to avoid geometrical losses due to the presence of a vacuum gap between the target and converter. Second, the establishing of the TNSA process is not allowed. Indeed, in TNSA, a small part of the electron energy would be transferred to ions with a modest reduction of photon generation due to electron BS. Moreover, the proposed configuration is very robust from the structural point of view. Compared to DLTs made by thin substrates, an mm-thick target does not require encapsulation in a perforated holder. The laser can be moved and focused quickly on the surface aiding the high repetition rate operation. Lastly, such a target-converter artifact can be easily manufactured. For instance, a near-critical carbon foam could be directly deposited on the surface of a tungsten plate via pulsed laser deposition<sup>32</sup>.

To simulate the electron generation in the near-critical layer, we perform a 3D PIC simulation. Technical details are provided in the “Methods” Section. Including a slice of the converter behind the near-critical density layer in the PIC simulation would require unbearable computational resources. Indeed, the slice should be thick enough to avoid the electron expansion at the rear side of the DLT. Moreover, because of the high density of the W converter, a huge number of macroparticles per cell and high spatial resolution would be needed. Therefore, we simulate only



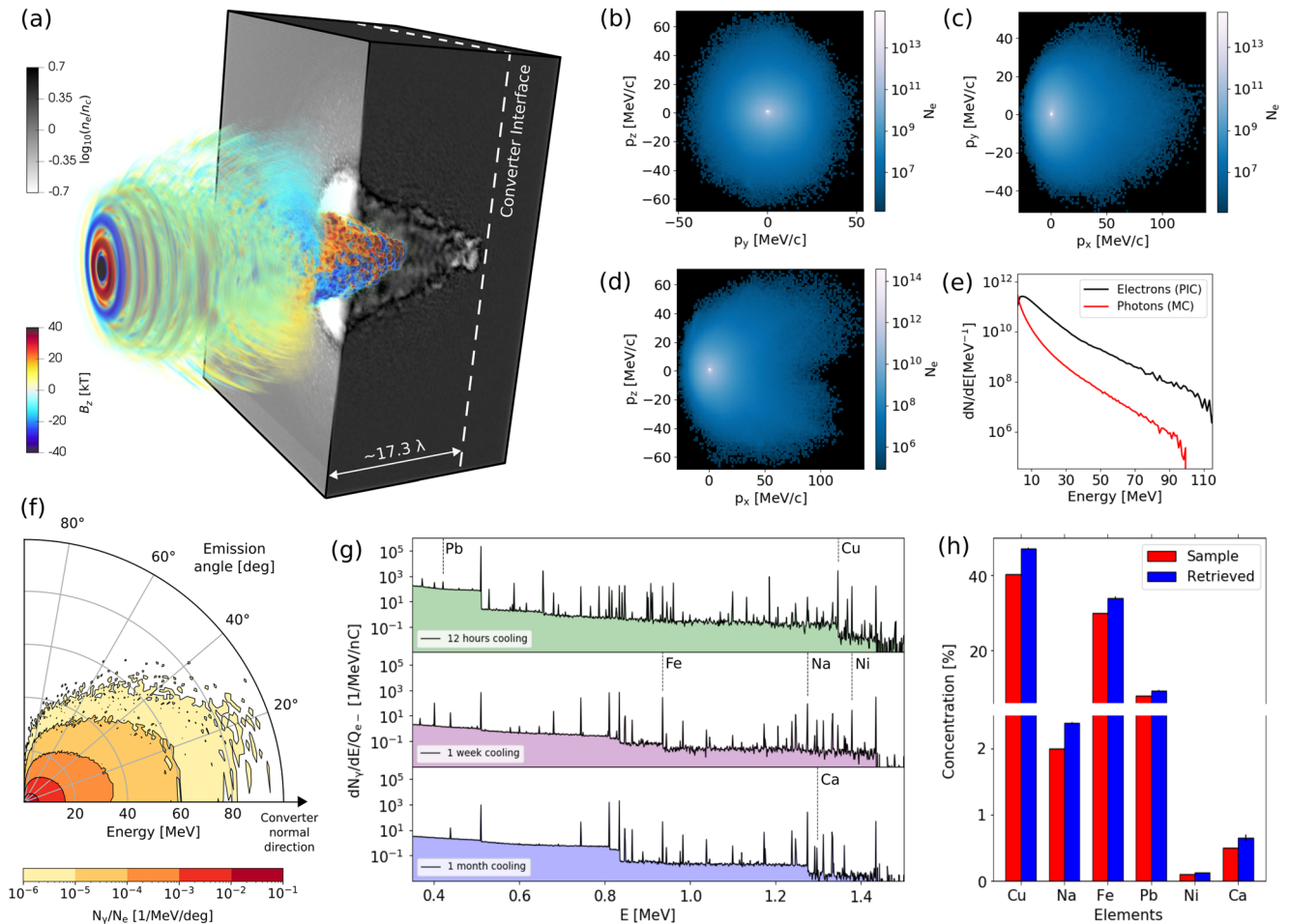


**Fig. 6 Results of the particle-in-cell and Monte Carlo simulations of Laser-driven PAA.** **a** Exploded view of the electron density and z-component of the magnetic field from the PIC simulation. They are retrieved at the instant of time in which the laser front is in correspondence with the rear side (the dashed white line) of the near-critical layer. **b–d** Momenta distributions of the electrons from the PIC simulation. The distributions are integrated along one direction in phase space and plotted in the other two. **e** Electron energy spectrum from the PIC and BS photon spectrum from MC. **f** Polar plot showing the angular divergence of the BS photons against their energy (i.e., the radial coordinate). The color map represents the number of photons normalized to the number of incident electrons. **g** Simulated photon spectra emitted following the activation of the sample. They are recorded after three different cooling times. **h** Comparison between the retrieved elemental concentrations and the values set in the MC simulation.

the near-critical medium and, to avoid the electron expansion in a vacuum, we set a thickness larger (i.e., equal to  $20\lambda$ ) than the actual value of  $17.34\lambda$ . The electron density and the z-component of the magnetic field at 166 fs after the start of the simulation are reported in Fig. 6(a). While part of the field is reflected during the interaction, the laser undergoes self-focusing digging a channel in the plasma. As it is shown in the figure, the laser front is at a distance equal to  $17.34\lambda$  from the laser-target interaction surface. Therefore, the electron momenta distribution  $d^3N/dp_x dp_y dp_z$  is retrieved at this instant of time and no further propagation is considered.

The  $d^2N/dp_x dp_y$  distributions integrated along the missing component are shown in Fig. 6(b–d). Differently from electrons exploited in conventional PAA, they are characterized by a broad momenta distribution. The distribution is symmetric in the  $p_y$ – $p_z$  plane, while they are forward peaked in the  $p_x$  component (which corresponds to the laser propagation direction). Figure 6(e) shows the electron energy spectrum. The resulting temperature of  $\sim 7.8$  MeV is in good accordance with the value of 7.5 MeV predicted by the model developed by Pazzaglia et al.<sup>51</sup>. About 60% of the total laser energy (equal to 8.6 J) is transferred to the electrons. We evaluate the number of accelerated electrons as the ratio between the total energy transferred to the electrons and the

temperature. The result is equal to  $4 \times 10^{12}$ , which is again in agreement with the value obtained from the model (equal to  $6.4 \times 10^{12}$ ). The PIC simulation does not consider the presence of the dense converter. On the other hand, the laser reflection at the converter surface is taken into account by the model (see the “Methods” Section). The agreement suggests that, under the present conditions, the effects at the interface are negligible compared to the volumetric heating occurring in the near-critical layer.

Then, we provide the momenta distribution from the PIC to the MC to properly simulate the BS photon production in the converter, the sample and standard activation and characteristic  $\gamma$ -rays emission. The BS spectrum is shown in Fig. 6(e). As expected, it has an exponential-like shape and the maximum energy extends above 90 MeV. As in the case of conventional PAA<sup>56</sup>, the photons interacting with the sample are characterized by a broad angular distribution, which is peaked in the forward direction (see Fig. 6(f)). The maximum angular aperture is  $\sim 20^\circ$  for the highest energy photons and it rises progressively up to  $\sim 80^\circ$  for energies lower than 20 MeV. The angular aperture is larger compared to that observed in conventional PAA<sup>4</sup> because of the broad electron momenta distribution. As a result, assuming the same sample-converter distance, laser-driven PAA is

**Table 2 Elemental mass concentrations in the sample and calibration material.**

Element	Cu	Ca	Ni	Ma	Cl	Fe	Pb	Z	Al	Si	Na	Po
Sample	0.404	0.005	0.001	0.01	0.012	0.3	0.08	0.11	0.02	0.028	0.02	0.01
Calibration material	0.33	0.0137	0.0003	0.006	0.036	0.025	0.19	0.074	0.047	0.018	0.015	0.02

characterized by more uniform irradiation conditions compared to conventional PAA. The same consideration holds also for the electrons not completely absorbed by the converter. With respect to conventional PAA, this condition can allow reducing the converter-sample distance, and therefore increase the photon flux, while maintaining uniform irradiation and avoiding over-heating of the material under investigation.

Figure 6(g) reports the characteristic  $\gamma$ -ray spectra recorded after 3 h of irradiation at 10 Hz repetition rate and 12 h, 1 week and 1 month cooling times. The characteristic peaks emerge over the background. As in the case of conventional PAA, several peaks disappear for longer cooling times. This allows avoiding spectral interference and better identify the corresponding elements. Exploiting the  $\gamma$ -ray line intensities  $N_{\gamma,s}^i$  and  $N_{\gamma,c}^i$  from both the sample and calibration material, respectively, we can reconstruct the sample elemental concentrations  $W_s^i$  originally set in the MC simulation as  $W_s^i = W_c^i N_{\gamma,s}^i / N_{\gamma,c}^i$ . The index  $i$  refers to the different elements and  $W_c^i$  are the elemental concentrations in the calibration material. The comparison between the retrieved and original elemental concentrations is shown in Fig. 6(h). Overall, the agreement is excellent, suggesting that the proposed laser-driven source could be exploited for PAA quantitative analysis. For all the elements, the predicted concentrations slightly overestimate the actual ones. This is ascribable to the fact that the sample is placed in front of the calibration material in the MC simulation. Therefore, the photon flux seen by the calibration material is partially attenuated by the sample. This effect can be avoided by exploiting a flux monitor, as already done in conventional PAA<sup>2</sup>.

The coupled PIC-MC simulation presented in this Section provides the first important evidence that state-of-the-art laser technology is suitable for laser-driven PAA. Nevertheless, a deeper study, involving several simulations, is required to identify the minimum range of laser parameters necessary for the technique. This could be the subject of a dedicated work.

## Conclusions

Laser-driven particle acceleration is of great interest as a potential multifunctional tool for the elemental analysis of materials. Indeed, these sources offer the unique possibility of accelerating different particles (e.g., ions, electrons, neutrons, and photons) at high energies. In this work, we have shown that super-intense lasers and near-critical targets can be exploited to generate high-energy photons suitable for photon activation analysis. We have proposed a theoretical framework to fully describe laser-driven PAA. We have identified the optimal target and converter parameters in a wide range of laser intensities. In addition, the model has been applied to assess the performance of the proposed configuration in terms of activated nuclei. Working at a high repetition rate (i.e., 1–10 Hz) is the main challenge to be addressed in order to achieve the capabilities of conventional PAA. It is worth mentioning that our approach can be useful also to assess the potential of a laser-based photon source for other interesting applications like radioisotopes production. Lastly, by means of relatively realistic simulations, we have shown that the state-of-the-art laser technology (i.e., intensity  $I \geq 5 \times 10^{20} \text{ W cm}^{-2}$ , time duration  $\sim 30 \text{ fs}$  and energy  $\sim 1\text{--}10 \text{ J}$ ) is suitable to carry out laser-driven PAA. While the main laser-driven

elemental analysis techniques investigated until now allow probing the sample surface (e.g., PIXE), laser-driven PAA can be used to analyze the multielemental composition of bulk materials. Therefore, the subject of this study represents an important step toward the development of a multiradiation platform for complementary materials science studies.

## Methods

**Monte Carlo.** We performed several Monte Carlo simulations exploiting the Fluka MC code<sup>50</sup>. The first set of simulations involved the BS production of  $\gamma$ -rays. The primary monoenergetic electrons are defined with the BEAM and BEAMPOS cards. On the other hand, when the input energy spectrum is nonmonoenergetic, a user routine (source.f) coupled with the SOURCE card is exploited. The tungsten converter has a parallelepipedal shape. Associated with this volume, we activate the EMFCUT card. This option allows us to reduce the computational time by setting 1 MeV and 100 keV energy thresholds for the pair and photon production, respectively. With the USRBDX card, we retrieve both the photon energy spectra and the double differential photon spectra in energy and solid angle. All the BS simulations are performed with  $10^7$  primary events per cycle and five cycles.

As far as the simulation of the sample and standard material activation is concerned, we provide the primary  $\gamma$ -ray energy spectrum to the MC by sampling from the BS photon energy distribution. Since no photonuclear reactions of interest can take place below 5 MeV electron energy, the primary photons are extracted above this threshold. The sample and calibration materials are placed one in front of the other at 10 cm from the source point separated by a 1 mm gap. They are two slabs of thicknesses equal to 3 mm and infinitely extended in the orthogonal plane. Their elemental mass concentrations are reported in Table 2. We activate again the EMFCUT for both the sample and standard material. Then, we activate the PHOTONUC card to switch on the photonuclear reactions. To further enhance the statistical accuracy of the results, biasing is performed using the LAMBIAS card. This allowed us to reduce the mean free path of photons by a factor of  $10^{-3}$ . The radioactive decay is carried out by exploiting the RADDECAY card. We also activate the PHYSICS card with the EVAPORAT option, which describes the decay with the evaporation model considering also heavy fragment evaporation. The irradiation conditions (i.e., current of primary particles and duration) are set through the IRRPROFILE card.

In order to acquire the characteristic  $\gamma$ -ray spectra collected during a certain measurement time, we exploit the DCYTIMES and USRBDX cards. Since Fluka does not allow us to automatically obtain energy spectra integrated along with a certain time interval, we record the activity at many times within the overall measurement period. The instants at which we retrieve the activity are defined with the DCYTIMES card. We associate a USRBDX card to each instant to get the photon energy spectra emitted from the sample and standard per unit time. Then, we integrate those spectra in the time variable to obtain the signal collected during the whole measurement period. It is worth pointing out that this procedure is reliable only if the time sampling is much smaller compared to the shorter half-life for the considered activated isotopes.

**Model for the laser interaction with a near-critical plasma.** The model proposed in<sup>51</sup> allows us to describe the propagation of a super-intense laser pulse in a uniform near-critical plasma and the generation of hot electrons. The presence of the nanostructure is not taken into account. The converter is considered as a high-density medium, in which the laser cannot propagate and only be reflected. Here, we provide a summary of the formulas we exploited in the first part of the “Results and discussion” Section. The laser pulse temporal profile is described with a  $\cos^2$  function and a Gaussian transverse shape. To model the self-focusing effect, the evolution of the beam waist  $w(r)$  along the propagation direction  $r$  (i.e., the depth in the near-critical layer) is treated exploiting the thin-lens approximation:

$$\frac{w(\bar{r})}{\lambda} \approx \sqrt{\frac{1}{\pi^2 \bar{n}} + \left(\bar{r} - \frac{w_0}{\lambda}\right)^2} \quad (5)$$

where  $\bar{r} = \sqrt{\bar{n}r/\lambda}$  is a normalized space variable,  $\lambda$  is the laser wavelength and  $\bar{n} = n_{nc}/\gamma_0 n_c$  is a relativistic transparency factor.  $\gamma_0 = \sqrt{1 + a_0^2/\varphi}$  is the average Lorentz factor of the electron motion (with  $\varphi$  equal to one and two for circular and linear polarization, respectively). Here, the hypotheses are that the beam waist during the propagation in the plasma  $w_m$  is significantly smaller compared to the initial one  $w_0$  and it keeps large compared to  $\lambda$ . During the propagation, the pulse heats the electrons and loses energy according to the ponderomotive scaling. The

normalized energy loss can be described as:

$$\frac{1}{\epsilon_{p0}} \frac{d\epsilon_p(r)}{dr} = -2 \left( \frac{2}{\pi} \right)^{3/2} V_2 C_{nc} \frac{1}{\tau c a_0 n_c} \frac{n}{a_0} \frac{\gamma(r) - 1}{w_0} \left( \frac{\beta w(r)}{w_0} \right)^2 \quad (6)$$

where  $\epsilon_{p0} = \pi^{3/2} 2^{-3/2-1} m_e c^2 n_e a_0^2 w_0^{3-1} \tau c$  is the initial energy of the Gaussian pulse in three dimensions,  $\tau$  is the field temporal duration,  $V^2$  is the volume of a 2-dimension hypersphere with a unitary radius,  $C_{nc}$  is a constant accounting for the details of the electron heating,  $\gamma_r = \sqrt{1 + a(r)^2/\varphi}$  is the local value of the Lorentz factor.  $\beta$  is the ratio of the plasma channel radius to the waist assumed to be constant. To solve equation (6), the pulse amplitude along the propagation length  $a(r)$  is obtained from:

$$a_0(r) = a_0 \sqrt{\frac{\epsilon_p(r)/\epsilon_{p0}}{(w(r)/w_0)^2}} \quad (7)$$

Equations (7) and (6) describe the pulse propagation in the near-critical plasma, and they are solved numerically with a finite difference method. In<sup>51</sup>, the free parameters  $\beta$  and  $C_{nc}$  are evaluated by fitting the data obtained with 2D-PIC simulations with the model.

To describe the evolution of the hot electron population, it is assumed that all the energy lost by the pulse is absorbed by the electrons. This hypothesis is valid for short laser pulses (tens of fs) and  $a_0 < 50$ . The fraction of laser energy given to the electrons is:

$$\eta_{nc}(r) = \epsilon_p(r)/\epsilon_0 - R_D \quad (8)$$

where  $R_D$  is the reflectance of the plasma. The evaluation of  $R_D$  is not trivial, since its value depends on the considered region of the pulse. Indeed, close to the laser peak, the electrons are relativistic and the plasma is near-critical allowing the pulse propagation. On the other hand, in close proximity to tails, the electrons can be nonrelativistic, resulting in an overcritical reflecting plasma. Considering the mentioned effects, an analytical expression for  $R_D$  in three dimensions is:

$$R_{3D} = \text{erf}(\sqrt{-2 \log \bar{n}}) \frac{4}{\sqrt{2\pi}} \bar{n}^2 \sqrt{-\log \bar{n}} \quad (9)$$

The number of hot electrons in the near-critical layer  $N_{nc}(r)$  is given by:

$$\frac{dN_{nc}(r)}{dr} = V_2 n_{nc} (\beta w(r))^2 \quad (10)$$

From equations (8) and (10) the hot electron energy results  $E_{nc}(r) = \eta_{nc}(r) \epsilon_{p0} / N_{nc}(r)$ . When the pulse reaches the substrate, it generates hot electrons at the interface  $r_{nc}$  with energy:

$$E_s(r_{nc}) = C_s (\gamma(r_{nc}) - 1) m_e c^2 \quad (11)$$

where  $C_s$  collects all the effects at the interface. As far as the absorption efficiency at the interface is concerned, it can be expressed as  $\eta_s = N_s(r_{nc}) E_s(r_{nc}) / \epsilon_p(r_{nc}) = 0.00388 a_0 + 0.0425$ , where the coefficients of the linear relation are obtained from PIC simulations. Then, the overall electron energy  $T_e(r_{nc})$  is obtained by combining the contributions of near-critical and substrate populations:

$$T_e(r_{nc}) = \frac{\eta_s \epsilon_p(r_{nc}) + \eta_{nc}(r_{nc}) \epsilon_{p0}}{N_e(r_{nc})} \quad (12)$$

where:

$$N_e(r_{nc}) = N_s(r_{nc}) + N_{nc}(r_{nc}) \quad (13)$$

is the total number of electrons. In our work, we use this model to obtain  $T_e$  and  $N_e$  defined in formulas (12) and (13) for different values of  $a_0$ ,  $r_{nc}$  and  $n_{nc}$ .

As already mentioned, the near-critical plasma is assumed to be uniform (i.e., the nanostructure of the foam or the presence of nanotubes is not considered). The effect of the nanostructure on electron acceleration was already studied exploiting PIC simulations<sup>65</sup>. Both homogeneous, fully and partially homogenized (as a result of the preheating induced by a prepulse) nanostructures were considered. For laser intensities comparable with that exploited in this work (i.e.,  $a_0 = 15$  and 45), Fedeli et al.<sup>65</sup> do not report significant variation in terms of electron temperature. On the other hand, a decrease of the maximum electron energy (e.g., from 150 MeV to 130 MeV for the  $a_0 = 15$ ,  $n_e = n_c$  case study) was observed with the nanostructure compared to the homogeneous case. The reduction is milder when a preplasma partially fills the gaps between nanoparticles. Such deviations, due to the nanostructure and prepulse, should not affect the analysis presented in this work because a negligible amount of photons are generated by the highest energy electrons.

**Particle-in-cell (PIC) simulation.** The 3D particle-in-cell (PIC) simulation was performed with the open-source code WarpX<sup>66</sup>. We exploited a computational box of  $75\lambda \times 75\lambda \times 75\lambda$  with a spatial resolution of 20 points per  $\lambda$  in all directions, where  $\lambda = 800$  nm. The time resolution was set at 98% of the Courant Limit. The laser was linearly polarized in the simulation plane, its transverse and longitudinal profiles were Gaussian. The laser  $a_0$  was 20.5, the waist was 4.7  $\mu\text{m}$  and the time duration was 30 fs. The incidence angle was 0°. The target consisted of a 2.5  $\lambda$  thick foil with a density of 2.92  $n_c$ . It was sampled with four macro-electrons and two

macro-ions with  $Z = 6$  and  $A = 12$ . The plasma was fully preionized and the electron population was initialized with a Maxwell-Boltzmann momentum distribution and temperature equal to 10 eV to avoid numerical artefacts. The ion population was initialized cold. The front target-vacuum interface was at 25  $\lambda$ . The duration of the simulation was 300 fs and the total number of simulated time steps was 4640. We retrieved the electric and magnetic laser field components, electron density and macro-electrons momenta every 105-time steps. The simulation was performed on the Marconi100 supercomputer of the Cineca consortium. We exploited 800 NVIDIA Volta V100 GPUs together with  $2 \times 400$  cores IBM POWER9 AC922 CPUs. The computation time was equal to  $\sim 1$  h.

## Data availability

The data supporting the findings of this work are available from the corresponding authors on reasonable request.

## Code availability

The codes generated during and/or analyzed during the current study are available from the corresponding author on reasonable request.

Received: 18 February 2021; Accepted: 23 July 2021;

Published online: 19 August 2021

## References

- Segebadé, C., Weise, H.-P. & Lutz, G. J. *Photon activation analysis* (Walter de Gruyter, 1987).
- Segebadé, C. & Berger, A. *Photon activation analysis* (John Wiley, 2006).
- Segebadé, C., Starovoitova, V. N., Borgwardt, T. & Wells, D. Principles, methodologies, and applications of photon activation analysis: a review. *J. Radioanal. Nucl. Chem.* **312**, 443–459 (2017).
- Starovoitova, V. & Segebadé, C. High intensity photon sources for activation analysis. *J. Radioanal. Nucl. Chem.* **310**, 13–26 (2016).
- Verma, H. R. *Atomic and nuclear analytical methods* (Springer, 2007).
- Benningshoven, A., Rudenauer, F. & Werner, H. W. Secondary ion mass spectrometry: basic concepts, instrumental aspects, applications and trends (Wiley, 1987).
- Shindo, D. & Oikawa, T. *Analytical electron microscopy for materials science*, 81–102 (Springer, 2002).
- Řanda, Z. & Kučera, J. Trace elements in higher fungi (mushrooms) determined by activation analysis. *J. Radioanal. Nucl. Chem.* **259**, 99–107 (2004).
- Ebihara, M. et al. How effectively is the photon activation analysis applied to meteorite samples? *J. Radioanal. Nucl. Chem.* **244**, 491–496 (2000).
- Řanda, Z., Kučera, J., Mizera, J. & Frána, J. Comparison of the role of photon and neutron activation analyses for elemental characterization of geological, biological and environmental materials. *J. Radioanal. Nucl. Chem.* **271**, 589–596 (2007).
- Masumoto, K. et al. Photon activation analysis of iodine, thallium and uranium in environmental materials. *J. Radioanal. Nucl. Chem.* **239**, 495–500 (1999).
- Kato, T., Sato, N. & Suzuki, N. Multielement photon activation analysis of biological materials. *Analytica. Chimica. Acta.* **81**, 337–347 (1976).
- Reimers, P., Lutz, G. & Segebadé, C. The non-destructive determination of gold, silver and copper by photon activation analysis of coins and art objects. *Archaeometry.* **19**, 167–172 (1977).
- Leonhardt, J. et al. Coal analysis by means of neutron-, gamma activation analysis and x-ray techniques. *J. Radioanal. Chem.* **71**, 181–187 (1982).
- Macchi, A., Borghesi, M. & Passoni, M. Ion acceleration by superintense laser-plasma interaction. *Rev. Mod. Phys.* **85**, 751 (2013).
- Daido, H., Nishiuchi, M. & Pirozhkov, A. S. Review of laser-driven ion sources and their applications. *Rep. Prog. Phys.* **75**, 056401 (2012).
- Corde, S. et al. Femtosecond x rays from laser-plasma accelerators. *Rev. Mod. Phys.* **85**, 1 (2013).
- Esarey, E., Schroeder, C. & Leemans, W. Physics of laser-driven plasma-based electron accelerators. *Rev. Mod. Phys.* **81**, 1229 (2009).
- Alejo, A. et al. Recent advances in laser-driven neutron sources. *Il Nuovo Cimento C.* **38**, 1–7 (2015).
- Passoni, M. et al. Advanced laser-driven ion sources and their applications in materials and nuclear science. *Plasma Phys. Control. Fusion.* **62**, 014022 (2019).
- Barberio, M., Veltri, S., Scisciò, M. & Antici, P. Laser-accelerated proton beams as diagnostics for cultural heritage. *Sci. Rep.* **7**, 40415 (2017).
- Passoni, M., Fedeli, L. & Mirani, F. Superintense laser-driven ion beam analysis. *Sci. Rep.* **9**, 1–11 (2019).
- Mirani, F. et al. Integrated quantitative pxe analysis and edx spectroscopy using a laser-driven particle source. *Sci. Adv.* **7**, eabc8660 (2021).
- Kishon, I. et al. Laser based neutron spectroscopy. *Nucl. Instrum. N Methods Phys. Res.* **932**, 27–30 (2019).



25. Ceccotti, T. et al. Proton acceleration with high-intensity ultrahigh-contrast laser pulses. *Phys. Rev. Lett.* **99**, 185002 (2007).
26. Zeil, K. et al. Robust energy enhancement of ultrashort pulse laser accelerated protons from reduced mass targets. *Plasma Phys. Control. Fusion*. **56**, 084004 (2014).
27. Ceccotti, T. et al. Evidence of resonant surface-wave excitation in the relativistic regime through measurements of proton acceleration from grating targets. *Phys. Rev. Lett.* **111**, 185001 (2013).
28. Passoni, M. et al. Toward high-energy laser-driven ion beams: nanostructured double-layer targets. *Phys. Rev. Accel. Beams*. **19**, 061301 (2016).
29. Prencipe, I. et al. Development of foam-based layered targets for laser-driven ion beam production. *Plasma Phys. Control. Fusion* **58**, 034019 (2016).
30. Bin, J. et al. Enhanced laser-driven ion acceleration by superponderomotive electrons generated from near-critical-density plasma. *Phys. Rev. Lett.* **120**, 074801 (2018).
31. Fedeli, L. et al. Structured targets for advanced laser-driven sources. *Plasma Phys. Control. Fusion* **60**, 014013 (2017).
32. Zani, A., Dellasega, D., Russo, V. & Passoni, M. Ultra-low density carbon foams produced by pulsed laser deposition. *Carbon*. **56**, 358–365 (2013).
33. Ma, W. et al. Directly synthesized strong, highly conducting, transparent single-walled carbon nanotube films. *Nano Lett.* **7**, 2307–2311 (2007).
34. Cialfi, L., Fedeli, L. & Passoni, M. Electron heating in subpicosecond laser interaction with overdense and near-critical plasmas. *Phys. Rev. E*. **94**, 053201 (2016).
35. Rosmej, O. et al. Interaction of relativistically intense laser pulses with long-scale near critical plasmas for optimization of laser based sources of mev electrons and gamma-rays. *N. J. Phys.* **21**, 043044 (2019).
36. Rosmej, O. et al. High-current laser-driven beams of relativistic electrons for high energy density research. *Plasma Phys. Control. Fusion* **62**, 115024 (2020).
37. Willingale, L. et al. The unexpected role of evolving longitudinal electric fields in generating energetic electrons in relativistically transparent plasmas. *N. J. Phys.* **20**, 093024 (2018).
38. Stoyer, M. et al. Nuclear diagnostics for petawatt experiments. *Rev. Sci. Instr.* **72**, 767–772 (2001).
39. Günther, M. et al. A novel nuclear pyrometry for the characterization of high-energy bremsstrahlung and electrons produced in relativistic laser-plasma interactions. *Phys. Plasmas*. **18**, 083102 (2011).
40. Malka, V. et al. Principles and applications of compact laser-plasma accelerators. *Nat. Phys.* **4**, 447–453 (2008).
41. Leemans, W. P. et al. Gev electron beams from a centimetre-scale accelerator. *Nat. Phys.* **2**, 696–699 (2006).
42. Kim, H. T. et al. Enhancement of electron energy to the multi-gev regime by a dual-stage laser-wakefield accelerator pumped by petawatt laser pulses. *Phys. Rev. Lett.* **111**, 165002 (2013).
43. Gonsalves, A. et al. Petawatt laser guiding and electron beam acceleration to 8 gev in a laser-heated capillary discharge waveguide. *Phys. Rev. Lett.* **122**, 084801 (2019).
44. Maier, A. R. et al. Decoding sources of energy variability in a laser-plasma accelerator. *Phys. Rev. X*. **10**, 031039 (2020).
45. Gustas, D. et al. High-charge relativistic electron bunches from a khz laser-plasma accelerator. *Phys. Rev. Accel. Beams*. **21**, 013401 (2018).
46. Ledingham, K. & Galster, W. Laser-driven particle and photon beams and some applications. *N. J. Phys.* **12**, 045005 (2010).
47. Ben-Ismaïl, A. et al. Compact and high-quality gamma-ray source applied to 10  $\mu$  m-range resolution radiography. *Appl. Phys. Lett.* **98**, 264101 (2011).
48. Galy, J., Maučec, M., Hamilton, D., Edwards, R. & Magill, J. Bremsstrahlung production with high-intensity laser matter interactions and applications. *N. J. Phys.* **9**, 23 (2007).
49. Ledingham, K. & Norreys, P. Nuclear physics merely using a light source. *Contemp. Phys.* **40**, 367–383 (1999).
50. Ferrari, A. et al. Fluka: a multi-particle transport code (SLAC, 2005).
51. Pazzaglia, A., Fedeli, L., Formenti, A., Maffini, A. & Passoni, M. A theoretical model of laser-driven ion acceleration from near-critical double-layer targets. *Commun. Phys.* **3**, 1–13 (2020).
52. Birdsall, C. K. & Langdon, A. B. *Plasma physics via computer simulation* (CRC press, 2004).
53. Arber, T. et al. Contemporary particle-in-cell approach to laser-plasma modelling. *Plasma Phys. Control. Fusion*. **57**, 113001 (2015).
54. Findlay, D. Analytic representation of bremsstrahlung spectra from thick radiators as a function of photon energy and angle. *Nucl. Instrum. Methods Phys. Res.* **276**, 598–601 (1989).
55. Berger, M. J. & Seltzer, S. M. Bremsstrahlung and photoneutrons from thick tungsten and tantalum targets. *Phys. Rev. C*. **2**, 621 (1970).
56. Starovoitova, V. & Segebad, C. High intensity photon sources for activation analysis. *J. Radioanal. Nucl. Chem.* **310**, 13–26 (2016).
57. Danson, C. N. et al. Petawatt and exawatt class lasers worldwide. *High Power Laser Sci. Eng.* **7**, 03000e54 (2019).
58. Wang, Y. et al. 0.85 pw laser operation at 3.3 hz and high-contrast ultrahigh-intensity  $\lambda = 400$  nm second-harmonic beamline. *Opt. Lett.* **42**, 3828–3831 (2017).
59. Prencipe, I. et al. Targets for high repetition rate laser facilities: needs, challenges and perspectives. *High Power Laser Sci. Eng.* **5**, 03000E17 (2017).
60. Chagovets, T. et al. Automation of target delivery and diagnostic systems for high repetition rate laser-plasma acceleration. *Appl. Sci.* **11**, 1680 (2021).
61. Booth, N. et al. *Target Diagnostics Physics and Engineering for Inertial Confinement Fusion III*, vol. 9211, 921107 (International Society for Optics and Photonics, 2014).
62. Willis, C., Poole, P. L., Akli, K. U., Schumacher, D. W. & Freeman, R. R. A confocal microscope position sensor for micron-scale target alignment in ultra-intense laser-matter experiments. *Rev. Sci. Instr.* **86**, 053303 (2015).
63. Schwarz, J. et al. Debris mitigation techniques for petawatt-class lasers in high debris environments. *Phys. Rev. Spec. Top-Accel. Beams* **13**, 041001 (2010).
64. Maróti, B. et al. Characterization of a south-levantine bronze sculpture using position-sensitive prompt gamma activation analysis and neutron imaging. *J. Radioanal. Nucl. Chem.* **312**, 367–375 (2017).
65. Fedeli, L., Formenti, A., Bottani, C. E. & Passoni, M. Parametric investigation of laser interaction with uniform and nanostructured near-critical plasmas. *Eur. Phys. J. D*. **71**, 1–8 (2017).
66. Vay, J.-L. et al. Warp-x: a new exascale computing platform for beam-plasma simulations. *Nucl. Instr. Methods Phys. Res.* **909**, 476–479 (2018).
67. Brown, D. A. et al. Endf/b-viii. 0: The 8th major release of the nuclear reaction data library with cielo-project cross sections, new standards and thermal scattering data. *Nucl. Data Sheets*. **148**, 1–142 (2018).
68. Krausová, L., Mizera, J., Řanda, Z., Chvátíl, D. & Krist, P. Nondestructive assay of fluorine in geological and other materials by instrumental photon activation analysis with a microtron. *Nucl. Instr. Methods Phys. Res.* **342**, 82–86 (2015).
69. Eke, C., Boztosun, I., Dapo, H., Segebad, C. & Bayram, E. Determination of gamma-ray energies and half lives of platinum radio-isotopes by photon activation using a medical electron linear accelerator: a feasibility study. *J. Radioanal. Nucl. Chem.* **309**, 79–83 (2016).
70. Řanda, Z., Kučera, J. & Soukal, L. Elemental characterization of the new czech meteorite ‘moravka’ by neutron and photon activation analysis. *J. Radioanal. Nucl. Chem.* **257**, 275–283 (2003).
71. Randa, Z. et al. Instrumental neutron and photon activation analysis in the geochemical study of phonolitic and trachytic rocks. *Geostand Geoanal. Res.* **31**, 275–283 (2007).
72. Aliev, R., Gainullina, E., Ermakov, A., Ishkhanov, B. & Shvedunov, V. Use of a split microtron for instrumental gamma activation analysis. *J. Anal. Chem.* **60**, 951–955 (2005).
73. Hislop, J. & Williams, D. The determination of lead in biological materials by high-energy  $\gamma$ -photon activation. *Analyst*. **97**, 78–78 (1972).
74. Landsberger, S. & Davidson, W. F. Analysis of marine sediment and lobster hepatopancreas reference materials by instrumental photon activation. *Anal. Chem.* **57**, 196–203 (1985).

## Acknowledgements

This project has received funding from the European Research Council (ERC) under the European Union’s Horizon 2020 research and innovation programme (ENSURE grant agreement No 647554). We also acknowledge LISA and Iscra access schemes to MARCONI HPC machine at CINECA(Italy) via the project THANOS.

## Author contributions

F.M. prepared the manuscript, developed the theoretical model for the comparison between conventional and laser-driven PAA, carried out the Monte Carlo simulations and contributed to the PIC simulation. D.C. contributed to the preparation of the manuscript, the model development, and the Monte Carlo simulation. A.F. performed the PIC simulation and revised the manuscript. M.P. conceived the project, supervised all the activities, and revised the manuscript.

## Competing interests

The authors declare no competing interests.

## Additional information

Correspondence and requests for materials should be addressed to F.M.

Peer review information *Communications Physics* thanks Luis Silva, Mickael Grech and the other, anonymous, reviewer(s) for their contribution to the peer review of this work.

Reprints and permission information is available at <http://www.nature.com/reprints>

**Publisher’s note** Springer Nature remains neutral with regard to jurisdictional claims in published maps and institutional affiliations.





**Open Access** This article is licensed under a Creative Commons Attribution 4.0 International License, which permits use, sharing, adaptation, distribution and reproduction in any medium or format, as long as you give appropriate credit to the original author(s) and the source, provide a link to the Creative Commons license, and indicate if changes were made. The images or other third party material in this article are included in the article's Creative Commons license, unless indicated otherwise in a credit line to the material. If material is not included in the article's Creative Commons license and your intended use is not permitted by statutory regulation or exceeds the permitted use, you will need to obtain permission directly from the copyright holder. To view a copy of this license, visit <http://creativecommons.org/licenses/by/4.0/>.

© The Author(s) 2021